TECHNICAL PAPER

Investigations on mechanical properties and microstructural examination of activated TIG-welded nuclear grade stainless steel

S. Mohan Kumar[1] · S. Sankarapandian[2] · N. Siva Shanmugam[1]

Abstract

Nuclear grade austenitic stainless steel 321 contains titanium for severe corrosive conditions and is used for process equipment, aircraft exhaust manifolds and boiler shells. Taguchi-based grey relational analysis technique has been considered to optimize the input parameters for welding SS321 material using activated tungsten inert gas welding process. The optimized input parameters were identified from the multiple output responses, i.e. arc length of 3 mm, welding current of 220 Amps and welding speed of 120 mm/min ($A_1B_3C_1$). The analysis of the variance table was performed to calculate the importance of the input parameters in the weldment quality. Also, the influence of the heat input on the depth of penetration and bead width at different arc lengths has been studied. The mechanical integrity is evaluated in terms of tensile strength for base metal (BM) (621 MPa) and weld metal (WM) (624 MPa) specimens by conducting the uniaxial tensile test. The 180° bend test with WM sample revealed the ductility level and was free from fissures and cracks. Charpy impact test results depicted the toughness values of BM (123.17 J) and WM (113.46 J) samples. Microstructural investigations at the SS321 WM highlighted the existence of columnar and equiaxed dendrites in the fusion zone. Moreover, the formation of titanium carbide reduces the chances of weld decay. Ferrite number measurement shows that the amount of delta ferrite is higher in WM (5.9) than in BM (1.2). The existence of dimples and voids in the fractographic analysis of the failed specimens (tensile and impact) confirms the ductile type of failure.

Keywords A-TIG welding · SS321 · Taguchi-based GRA · Tensile properties · Microstructure examination

1 Introduction

SS321 is one of the noticeable grades of austenite stainless steel, which has general corrosion resistance and excellent protection from intergranular corrosion during temperature exposure in the precipitation range of chromium carbides in 800–1500 °F (427–816 °C) [1]. It has good mechanical integrity and erosion resistance at high temperatures. This grade of steel is suitable choice for diverse applications in structural components at nuclear reactors, oil refinery

equipment and exhaust systems in automobile [2]. Gas tungsten arc welding (GTAW) processes are the most popular manufacturing processes that are used for welding metals such as titanium alloys, stainless steel and aluminium alloys because of their high quality and welding economically. However, the main shortcoming of TIG welding process is that welding can be carried out up to certain plate thickness in a single pass [3]. To prevail over this limitation, a thin coating of flux is applied on the plate surface to be joined for achieving high DOP in a single pass (plates of 6 mm thick or more) trailed by TIG process, this method is widely distinguished from A-TIG welding process, and this incredible DOP is a result of the mechanisms such as arc constriction and reversal of Marangoni flow. The Paton Institute of Welding of the National Academy of Sciences of Ukraine developed the activated TIG welding or A-TIG welding in 1960 with the help of the flux [4]. In addition, the quality of the weld depends mainly on the mechanical integrity of the weldment and is influenced by the metallurgical properties and nominal composition of the WM. Also, these

---

✉ N. Siva Shanmugam
nsiva@nitt.edu

1   Department of Mechanical Engineering, National Institute of Technology, Tiruchirappalli, Tamil Nadu 620 015, India

2   Department of Mechanical Engineering, Alagappa Chettair Government College of Engineering and Technology, Karaikudi, Tamil Nadu 630 003, India

metallurgical and mechanical properties of welded joints are based on the geometry of the weld, directly related to the input parameters of the welding process. The quality of the welds depends mainly on the welding process and its input parameters [5]. Therefore, a number of process parameters come into the picture in a difficult manner which directly or indirectly impacts on weld bead profile, metallurgical properties and mechanical behaviour of the WM. There is a need to find an optimal process parameter for obtaining a desired quality weld. Hence, an optimization technique is applied so as to fulfil all the objectives to achieve a good-quality weld. Such a technique is named multi-response optimization technique [6]. Most of the researchers have used various multi-objective techniques such as principal component analysis, GRA, genetic algorithm and simulated annealing algorithm to optimize the input parameters. Optimization techniques such as simulated annealing and genetic algorithm require an appropriate function and more data, whereas GRA is quite simple and can be realistic even to small amount of data without any function [7]. Juang et al. [8] investigated the selection of parameters for the welding process to achieve the optimal weld geometry, such as the back height, back width, front height and front width using TIG process on austenitic grade steel and further have established a Taguchi technique to analyse the result of the input parameters on the geometry of the weld for optimum set of process parameters. Nagesh et al. [9] formulated a new approach for predicting the geometry of the weld bead with the aid of neural network and application of genetic algorithm to optimize the welding input process parameters in TIG process of 1100 aluminium material. Farhadkolahan et al. [10] derived the regression model for the Taguchi's experimental matrix design to create a correlation between input parameters such as arc length, welding speed, voltage, torch angle, rate of wire feed and output results from gas metal arc welding (GMAW) process, such as weld bead height, BW and DOP. Nandagopal et al. [11] have optimized TIG welding process parameters to weld dissimilar materials of aluminium 7075 and titanium 6Al4V with filler metal (aluminium 4047). In addition to that, they have derived analysis of variance technique to find out the percentage contribution by each welding input parameter and also examined metallurgical studies of weld samples. Pan et al. [12] have optimized the multiple quality characteristics of the titanium alloy plates welded with laser using the grey analysis based on Taguchi. Tamrin et al. [13] studied the optimized characteristics of the welds with CO_2 laser welding of dissimilar materials using GRA. They also obtained the ANOVA table to figure out the correlation between input process parameter and the characteristics of the welded joint. Kim et al. [14] developed a new method for the optimization of Nd:YAG laser and GMA hybrid and welding parameters such as wire feed rate, travelling speed, type of wire used, laser focus, laser power and

shielding gas using GRA. Padhi et al. [15] developed an optimization approach to find optimal process input parameters for laser welding to maximize weld bead depth and minimize BW of austenitic grade steel 304 sheets of 2.9 mm thick in pulsed laser welding using Taguchi-based GRA. Hsiao et al. [16] optimized the parameters of the welding process such as the plasma gas flow rate, the welding speed of the torch and the welding current of the plasma arc welding, taking into account the response from the performance characteristics, viz. the width of the welding groove, the weld pool undercut and the penetration of the root, using the Taguchi method with GRA. Saurabh Kumargupta et al. [17] studied optimization technique with multi-objective for welding input parameters using FSW of dissimilar alloys of aluminium AA5083/AA6063 material. Sefika Kasman [18] studied and optimized the dissimilar FSW input parameters such as welding speed, shoulder diameter-to-pin diameter ratio, tool rotational speed and tool that were related to tensile strength as well as percentage of elongation of AA6082/AA5754 aluminium alloys. Tarng et al. [19] used the Taguchi method based on the GRA to optimize the process parameters for hardfacing with submerged arc welding (SAW) process, taking into account the multiple qualities of welded joints. Joby Joseph et al. [20] established the optimal input process parameters of activated TIG welding of AISI 4135 type steel using simulated annealing and genetic algorithm. Dan Wu et al. [21] have studied the use of an orthogonal experiment in the A-TIG welding process in austenitic grade steel for butt joint of 8-mm-thickness plate. Ahmadi et al. [22] used Taguchi technique to evaluate the activating fluxes effect on the penetration depth of TIG welds using fluxes such as TiO_2 and SiO_2 and mechanical properties of AISI 316L steel. Patel et al. [23] have studied the influence of activating fluxes on weldment strength using Taguchi method with L_9 orthogonal array for AISI 321 steel using TIG process. Although most researchers have shown that ANOVA and Taguchi's experimental design techniques are the most predominant tools to analyse the effect of process parameters. In addition to that, the GRA has been executed extensively to find various responses from process parameters using the multiple performance optimization [24]. Based on the available literature, few papers have been published on the optimization of the input process parameters of A-TIG welding. Very few studies have been reported with the use of the Edison Welding Institute (EWI) flux in the TIG welding process of the SS321 steel. Therefore, in this research work, it is tried to optimize the input process parameters of the A-TIG welding using Taguchi-based GRA to achieve the preferred welding quality. The GRA optimization used in this study will give an idea to the industry regarding the parameters that has to be chosen in A-TIG welding of SS321 type steel. It can be broadly used in oil and gas industry for storing fluids, in chemical industry to handle hazardous

chemicals and in heat exchangers to transfer hot fluid. Hence, it will improve the productivity by reducing the time involved in choosing the right combination of input parameters and increase the quality by avoiding the defects in the weld. Also, it will help the researchers to understand the relation between DOP and the BW. Hence, researchers will be very aware of choosing the parameters. Further, the mechanical properties of A-TIG welding butt joint, (i.e. best and least GRG experiment) were validated with the help of microstructure and SEM fractographic analysis.

2 Materials and methods

The developed models are based on the trial-and-error experimentation. The factors considered for the experimentation and optimization are the AL, WC and WS.

2.1 Base metal

The present work is focused on SS321 steel plate of 6 mm thick. Before welding, the bead on a plate with a required size of $300 \times 110 \times 6$ mm was cut and scrubbed with wire brush and lightly rinsed with acetone. Table 1 displays the elemental composition of the candidate material SS321.

2.2 Experimental method

The A-TIG welding process is carried out on SS321 with the help of TIG machine of Fronius make with a torch head assisted by cooling water and numerical control (NC) unit to regulate the traverse speed of the torch as presented in Fig. 1. The combination of oxides present in the commercially available EWI flux and corresponding ranges are indicated in Table 2 [25–27].

From the available literature, it is understood that the AL, WC and WS are considered as process parameters as they play a significant role in evaluating the heat input and quality of the weldments. The selected experimental design for this work is based on an L_{27} orthogonal array to achieve the high DOP and corresponding BW for the A-TIG welding process of SS321. The activated flux was mixed with acetone and coated on the base metal surface with a width of 10 mm immediately prior to welding with the help of a brush. The

Table 1 Elemental composition of candidate material SS321 (weight percentage, wt%)

Element name	Mn	P	C	Ni	Cr	S	Si
Composition, %	1.007	0.031	0.032	9.356	17.560	0.016	0.349
Element name	Ti	Al	Mo	Cu	W	Nb	Fe
Composition, %	0.356	0.006	0.113	0.356	0.036	0.003	70.775

Fig. 1 A-TIG welding set-up
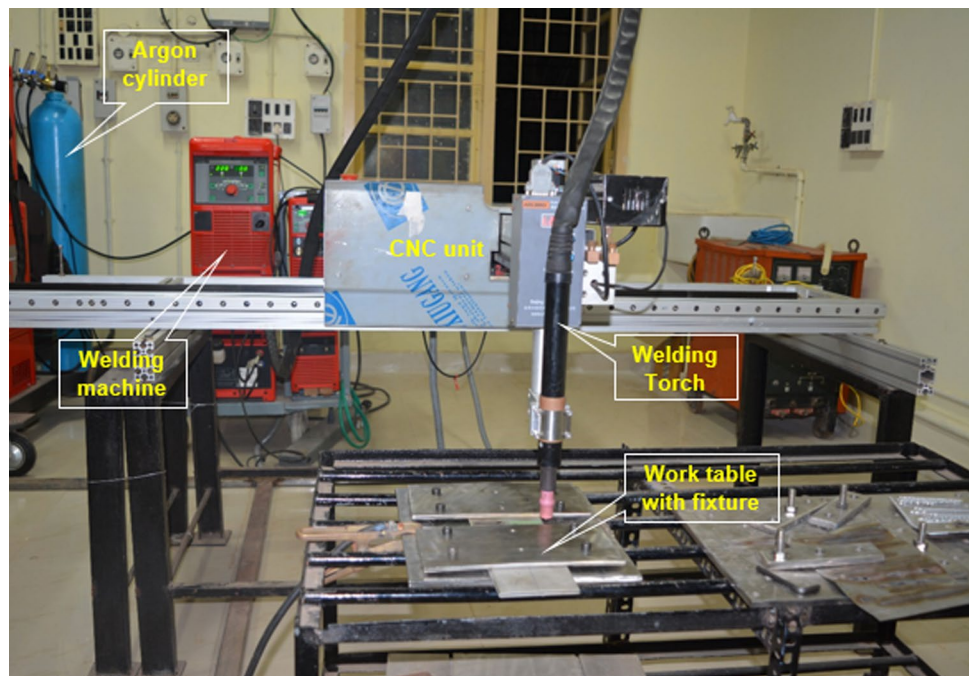
Table 2 EWI-flux composition

Name of the ingredients	Weight percentage
Chromium III oxide, Cr_2O_3	0–50
Silicon oxide, SiO_2	0–20
Titanium oxide, TiO_2	20–60

Table 3 Experimental welding input parameters (control factors and levels)

Factors (A, B and C)	Levels		
	1	2	3
AL, mm	3	4	5
WC, Amps	120	170	220
WS, mm/min	120	150	180

easily vapourable liquid evaporates to separate a thin film of coating that is satisfactorily adhered to the surface of the base metal to be joined. From the selected input parameters, the design matrix is established with three control factors and levels which are listed in Table 3. A total of 27 beads on plate weld trials are conducted with DCEN (direct current electrode negative) polarity in A-TIG welding process on

SS321 by keeping the shielding gas at a flow rate of 20 l/min (industrial standard 99.99% pure argon), and respective bead on the plate (27 trials) of base metal is presented in Fig. 2.

2.3 Preparation of sample for the measurement of weld bead geometry

After completion of the trials, the samples were sliced from plate using wire-cut EDM to obtain smooth edges of desired dimensions (Fig. 3). The samples are mounted and rubbed using various grades of sand papers and polished with alumina (Al_2O_3, 0.05 μm). With the help of electrolytic etching, the specimens were etched using a mixture of 10 ml oxalic acid in 100 ml of water for 50 to 60 s at a potential of 6 V for observing the weld bead geometry. The weld bead dimensions such as DOP and BW were measured for each sample with the aid of Struers welding expert system at a magnification of 20X. The measured weld characteristics are shown in Table 4.

3 Results and discussion

3.1 Taguchi technique

Japanese statistician Genichi Taguchi developed an orthogonal array (OA)-based method that is widely used

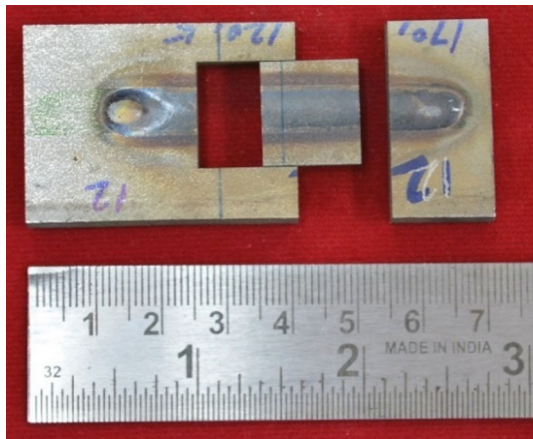**Fig. 2** Bead on plate trials in SS321 (27 trials)

Fig. 3 Specimen preparation (sample 22)

in various engineering fields to optimize process parameters [28]. In the Taguchi technique, process parameter optimization can be obtained through the integration of experimental design (DOE). OA provides an even-handed set of experiments, and the S/N ratio of Taguchi method is a logarithmic function of the preferred output parameters, used as an objective function of the optimization. It helps to inspect the whole parameter range with less number of experiments (minimal experimental trials) [5]. OA and *S/N* ratios are extensively applied to inspect the influences on the factors of noise and control and to evaluate good-quality features for the particular application [29]. Optimized process parameters achieved by the Taguchi method are tactless against changes in environmental circumstances and other factors of noise [30]. Initially, the Taguchi method was developed to optimize the performance feature of a single. However, optimizing multiple-performance features is not a direct and more complex than a single-performance feature. In order to evaluate the multi-performance feature problems, the Taguchi method is used along with the GRA [31]. Seminal on GRA was carried out by Deng [32] to reach key mathematical standards for in connection with deprived, deficient and doubtful systems [33]. This GRA-based Taguchi method has been extensively applied in various disciplines of engineering to evaluate the optimization problems with multiple responses.

Table 4 Bead on plate layout with L_{27} orthogonal array and corresponding result

Trial no.	AL, mm	WC, Amps	WS, mm/min	DOP, mm	BW, mm	Heat input, kJ/mm
1	3	120	120	2.2826	5.1827	0.6426
2	3	120	150	1.6326	4.8802	0.5356
3	3	120	180	1.3679	4.5583	0.4680
4	3	170	120	4.3235	7.1065	1.0404
5	3	170	150	3.2207	6.8408	0.8568
6	3	170	180	2.8086	6.5822	0.7344
7	3	220	120	6.0000	8.9770	1.4751
8	3	220	150	5.3904	7.6308	1.2117
9	3	220	180	4.8226	7.4575	1.0362
10	4	120	120	2.2286	5.0760	0.6318
11	4	120	150	1.5812	4.7901	0.5270
12	4	120	180	1.0728	4.3215	0.4608
13	4	170	120	3.7412	7.0693	1.0251
14	4	170	150	3.1652	6.7997	0.8506
15	4	170	180	2.6829	6.4526	0.7293
16	4	220	120	5.8325	8.9300	1.4553
17	4	220	150	5.1203	7.5839	1.1959
18	4	220	180	4.5281	7.4127	1.0230
19	5	120	120	2.0065	4.9203	0.6264
20	5	120	150	1.4944	4.6815	0.5184
21	5	120	180	0.8733	4.2356	0.4536
22	5	170	120	3.4676	6.8737	1.0098
23	5	170	150	2.9803	6.6506	0.8445
24	5	170	180	2.5986	6.3978	0.7242
25	5	220	120	5.5422	8.6849	1.4454
26	5	220	150	5.0993	7.5194	1.1880
27	5	220	180	4.4012	7.3131	1.0164

3.2 Grey relational analysis (GRA)

In GRA, black means no data or information and white, with all the data or information. Grey level of the data or information system is intermediate between black and white. It means that, in the grey system, some information is known and some are unknown [34]. The theory of Grey system avoids the innate restrictions of statistics, traditional techniques and only requires limited value or data to assess the behaviour of uncertain systems. The system is especially suited for data with multiple inputs, uncertainties and different attributes. With grey theory, systems can be inspected through grey relational grade (GRG), modelling, prediction and decision-making. Thus, using GRA, the GRG can be achieved to estimate the multiple-performance features, so that the optimal target of convoluted multiple-performance features can be converted to optimize the single GRG. The steps of GRA are as follows [35–37].

3.2.1 Grey relational generation

In the first step, the results of the experiments such as DOP and BW are normalized in the range of 0 and 1. This circumvents the problem of different units, scales and targets. There are various types of data normalization according to necessity the larger is better (LB), the smaller is better (SB) and nominal is better (NB). In case of activated TIG welding, the ultimate purpose is to increase the DOP at a minimal of BW, so that all heat input is efficiently used to penetrate the material as well as to achieve desired quality A-TIG weldments. Hence, the generation of the grey relation, the normalization of a characteristic, such as DOP, is a "larger-the-better" (LB) criterion, which can be stated by Eq. (1).

$$X_i^*(k) = \frac{y_i(k) - \min y_i(k)}{\max y_i(k) - \min y_i(k)}. \tag{1}$$

BW should satisfy the "smaller-the-better" (SB) criterion, which is described in Eq. (2) [28].

$$X_i^*(k) = \frac{\max y_i(k) - y_i(k)}{\max y_i(k) - \min y_i(k)} \tag{2}$$

where $i = 1, 2, 3,…m$; $k = 1$ to n; m = number of trial data and n = number of factors. $y_i(k)$ = original sequence for the kth response; $X_i^*(k)$ is the value after the generation of the grey relation; and $\max y_i(k)$ and $\min y_i(k)$ are the maximum and minimum value of $y_i(k)$ for the kth response, respectively. Supposing the ideal sequence $X_o^*(k)$ for the kth response, then its value will be the maximum value of this specific column, which will always be 1, and $\Delta_{oi}(k)$ is the difference between the absolute values of $X_o^*(k)$ and $X_i^*(k)$, that is, how much this specific value deviates from the ideal value,

which can be calculated from Eq. (3) [38]. The normalized and sequences values are indicated in Table 5.

$$\Delta_{0i}(k) = |X_0^*(k) - X_i^*(k)| \tag{3}$$

where $X_i^*(k)$ = corresponding normalized value of given set of input parameters.

3.2.2 Grey relational coefficient (GRC)

It gives the relation between the actual and ideal normalized experimental results. The GRC is calculated by Eq. (4)

$$\xi_i(k) = \frac{\Delta_{\min} + \xi \Delta_{\max}}{\Delta_{0i}(k) + \xi \Delta_{\max}} \tag{4}$$

where ξ is the identification or distinguishing coefficient: $\xi \in [0, 1]$. In this study, $\xi = 0.5$ is considered. $\Delta_{\max}$ = largest value of $\Delta_{oi}(k)$ and $\Delta_{\min}$ = smallest value of $\Delta_{oi}(k)$ [39].

Table 5 Normalization and sequences of each response characteristic after data processing

Trial no.	Normalization		Sequences	
	DOP, mm	BW, mm	DOP, mm	BW, mm
1	0.274894	0.800249	0.725106	0.199751
2	0.148107	0.864049	0.851893	0.135951
3	0.096475	0.931940	0.903525	0.068060
4	0.672987	0.394504	0.327013	0.605496
5	0.457877	0.450542	0.542123	0.549458
6	0.377494	0.505083	0.622506	0.494917
7	1	0	0	1
8	0.881093	0.283925	0.118907	0.716075
9	0.77034	0.320475	0.229660	0.679525
10	0.264361	0.822753	0.735639	0.177247
11	0.138081	0.883051	0.861919	0.116949
12	0.038914	0.981883	0.961086	0.018117
13	0.559405	0.402350	0.440595	0.597650
14	0.447052	0.459210	0.552948	0.540790
15	0.352976	0.532417	0.647024	0.467583
16	0.967328	0.009913	0.032672	0.990087
17	0.828408	0.293816	0.171592	0.706184
18	0.712895	0.329924	0.287105	0.670076
19	0.221039	0.855591	0.778961	0.144409
20	0.121150	0.905956	0.878850	0.094044
21	0	1	1	0
22	0.506037	0.443603	0.493963	0.556397
23	0.410986	0.490657	0.589014	0.509343
24	0.336532	0.543974	0.663468	0.456026
25	0.910703	0.061606	0.089297	0.938394
26	0.824312	0.307420	0.175688	0.692580
27	0.688142	0.350930	0.311858	0.649070

3.2.3 Grey relational grade (GRG)

The GRG is calculated by taking the mean of the GRC allied to every performance feature. The general calculation of multiple-performance features is depending on the GRG, i.e.

$$\gamma_i = \frac{1}{n} \sum_{k=1}^{n} \xi_i(k) \qquad (5)$$

where γ_i = GRG for the ith experiment trial and n = number of responses.

3.3 Optimization of activated TIG welding parameters

In the A-TIG welding, flux can be used to achieve higher DOP with single pass, so that the most desirable output, BW, is kept minimal. In this study, weighing factor used for DOP is 0.9 and for BW is 0.1 [8]. The weight has been assigned by considering the significance of these responses, in the high DOP achieving process like A-TIG welding. The assigned weight of grey relational coefficients and calculated grey relational grade are presented in Table 6. In addition, the GRG will be used to evaluate the *S/N* ratio values. Table 7 shows that the *S/N* ratio on the basis is larger which is the best criterion for the overall GRG calculated using Eq. (6).

$$S/N = -10 \log \left[\frac{1}{n} \sum_{i=1}^{n} \frac{1}{y_i^2} \right] \qquad (6)$$

where n = number of measurements and y_i = measured characteristic value.

　　Figure 4 shows the S/N ratio curve, which is a graphical illustration to examine optimized set of process parameters. In the *S/N* ratio graph, if the ratio is high, the desired effect is maximal with minimal noise. It follows from Fig. 4 that a higher *S/N* ratio is observed with an AL of 3 mm, a WC of 220 Amps and a WS of 120 mm/min. From the response mean in Table 8, it can be seen that the WC range is higher than the WS and AL, which confirms that the WC has the greatest influence among all other responses. So, based on the examinations, it also indicates the optimal set of parameters are $A_1 B_3 C_1$, i.e. Trial no. 7, which are given in Table 9. Figure 5 displays the optimized parameter weld bead surface and macrostructure of Trial no. 7 which is captured by a metallurgical microscope of 7X magnification.

3.4 ANOVA

The objective of the ANOVA lies in checking the most likely welding parameter that is significant in affecting

Table 6 GRC and GRG

Trial no.	GRC		GRG	Rank
	DOP, mm	BW, mm		
1	0.408128	0.714540	0.438769	19
2	0.369852	0.786224	0.411489	22
3	0.356246	0.880189	0.408640	25
4	0.604585	0.452286	0.589355	10
5	0.479790	0.476436	0.479455	13
6	0.445432	0.502554	0.451144	16
7	**1**	**0.333333**	**0.933333**	**1**
8	0.807876	0.411159	0.768204	4
9	0.685250	0.423899	0.659115	7
10	0.404649	0.738283	0.438012	20
11	0.367129	0.810440	0.411460	23
12	0.342211	0.965033	0.404493	26
13	0.531578	0.455518	0.523972	11
14	0.474857	0.480404	0.475412	14
15	0.435911	0.516751	0.443995	17
16	0.938664	0.335551	0.878352	2
17	0.744500	0.414531	0.711503	5
18	0.635239	0.427323	0.614448	8
19	0.390942	0.775905	0.429439	21
20	0.362621	0.841689	0.410528	24
21	0.333333	1	0.4	27
22	0.503037	0.473307	0.500064	12
23	0.459131	0.495372	0.462755	15
24	0.429750	0.522999	0.439075	18
25	0.848468	0.347610	0.798382	3
26	0.739986	0.419259	0.707914	6
27	0.615872	0.435135	0.597798	9

the performance characteristic (weld quality) [40]. This is achieved by the total variability of the GRG separation, which is the measure of the sum of the square deviations from the total mean of the GRG, towards improvement by each welding parameters and error [6]. Thus;

$$SS_T = SS_F + SS_e \qquad (7)$$

$$SS_T = \sum_{j=1}^{p} (\gamma_j - \gamma_m)^2 \qquad (8)$$

where SS_T = total sum of squared deviations from the mean, SS_F = the sum of squares of deviations due to each factor, SS_e = the sum of squared deviations due to an error, p = number of experiments in the orthogonal matrix, γ_m = grand mean value of the response and γ_j = mean response for the jth experiment.

　　In the ANOVA table, the mean of the square and the deviation F are defined as:

Table 7 Signal-to-noise ratio table

Trial no.	S/N ratio
1	−7.15528
2	−7.71284
3	−7.77318
4	−4.59246
5	−6.38505
6	−6.91369
7	−0.59926
8	−2.29047
9	−3.62077
10	−7.17027
11	−7.71344
12	−7.86177
13	−5.61383
14	−6.45860
15	−7.05245
16	−1.12662
17	−2.95647
18	−4.23030
19	−7.34198
20	−7.73315
21	−7.95880
22	−6.01949
23	−6.69298
24	−7.14923
25	−1.95578
26	−3.00039
27	−4.46891

$$\text{Mean Square} = \frac{\text{MS (Sum of square deviation)}}{\text{DOF (Degree of freedom)}} \qquad (9)$$

$$F \text{ ratio} = \frac{\text{Mean square for a term}}{\text{Mean square for the error term}}. \qquad (10)$$

Normally, the significance's probability is calculated depending on the value of F and P. In addition, an F-test was performed to determine process parameters that have a noteworthy influence on performance. Typically, changing the welding parameter will have a substantial effect on performance features at a high F value [41].

If the P value is lower than 0.05 (95% confidence), then it is established that the influence of the factors/interaction of the factors is significant in the selected response (using the MINITAB 17 software). It can be noted that the value of P for the WC and WS is less than 0.05. Obviously, WC and WS are the most important factors. The effect of other factors on the GRG seems to be insignificant. The best insignificant factor is converted into conditional random fields (Crf) for higher P value [5]. The percentage contributions of the input process parameters in the activated TIG welding are shown in Tables 10 and 11. The result of the ANOVA displays that the WC (87.0% influence) is the important parameter in the responses under multi-criteria optimization (DOP and BW). The percentage contributions of the other parameters are WS (11.6%) and AL (1.4%) [6].

3.5 Regression analysis

The arithmetical mean between the two or more process input parameters for the assessment is called a regression
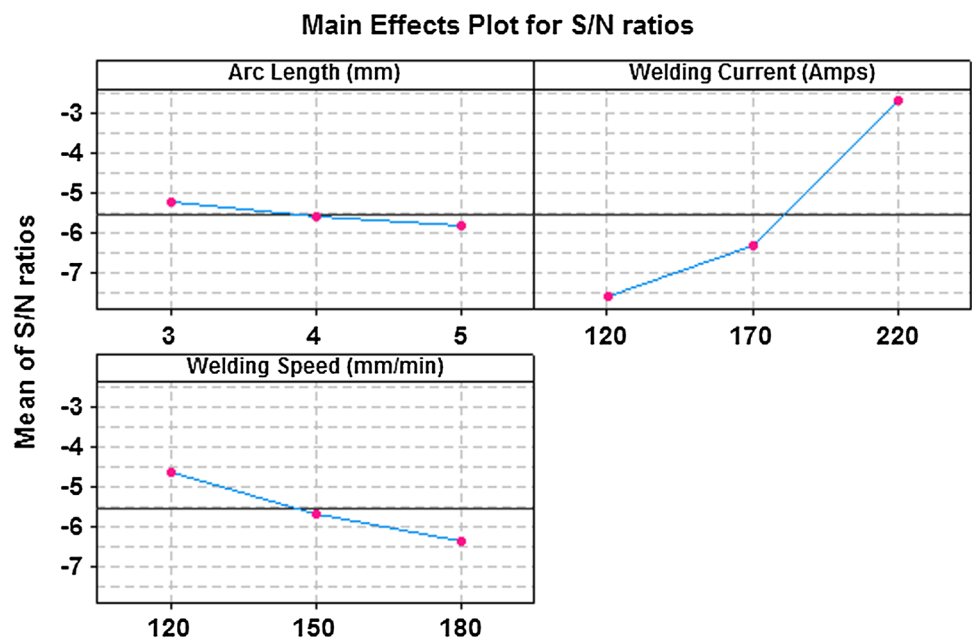
Fig. 4 Signal-to-noise ratio plot

Table 8 Response mean table for grey relational grade

Parameter/level	AL, mm	WC, Amps	WS, mm/min
Level 1	**0.5711**	0.4170	**0.6144**
Level 2	0.5446	0.4850	0.5376
Level 3	0.5273	**0.7410**	0.4910
Range (max–min)	0.0437	0.3240	0.1234
Rank	3	1	2

Table 9 Optimal set of input parameters (Trial no. 7)

AL, mm	WC, Amps	WS, mm/min
3	220	120

analysis [11, 42]. The regression analysis is carried out in this investigation for AL, WC and WS and to obtain the optimal set of parameters.

With a confidence level of 95%, the model was tested. Multiple linear regression models have been developed for grey relational grade with main factors of process parameters such as AL, WC and WS, which is given by,

$$GRG = 0.393 - 0.0219 * AL + 0.00324 * WC - 0.00206 * WS.$$

It can be perceived that the regression model has been developed as a function of the major process parameters and their interactions. Using the regression model, a data set (predicted value) has been constructed. The actual value

Table 11 Contribution percentage of the input parameters

Parameter	% of contribution
AL, mm	1.4
WC Amps	87.0
WS, mm/min	11.6

and the predicted value of GRG are reported in Table 12 and Fig. 6. The error deviation between experimental and predicted values of grey relational grade ranges between 0.32 and 32.67%. From this, it is inferred that the developed regression model for grey relational grade is 92.88% confidence level [18].

3.6 Heat input effect on DOP and BW

In the A-TIG welding process, DOP and BW are the most significant output responses to produce high-quality welds because they sturdily impact the changes in the base material. In addition, the heat input in the weldment mostly depends on the traverse speed, voltage and current. Hence, it is essential to determine the effect of thermal input on resultant output responses such as DOP and BW. Figures 7 and 8 show the typical deviation in the DOP and BW for various heat inputs on base material during A-TIG welding process at various arc lengths. The facts presented in the plots are characterized by a second-degree polynomial equation, and it indicates the excellent fit with R^2 values of 0.984, 0.9807 and 0.9698

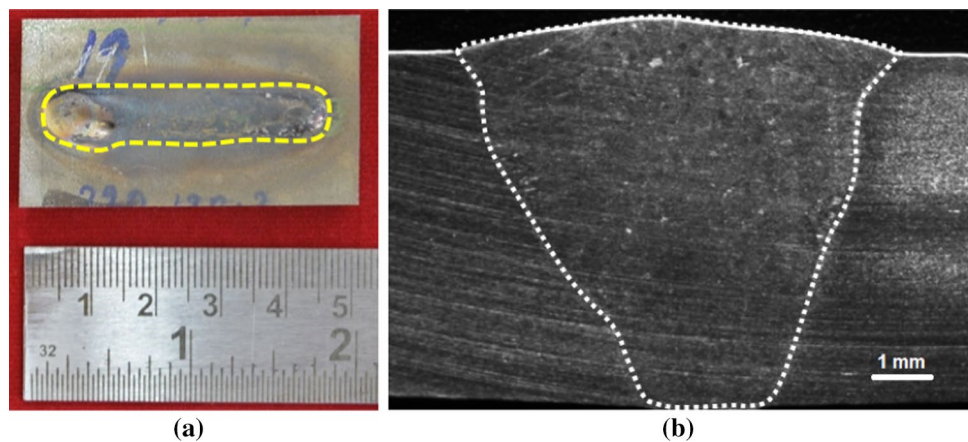**Fig. 5** Bead surface (**a**) and macrograph (**b**) obtained for optimized parameters (Trial no. 7)

Table 10 ANOVA table

Factor	DOF	Sum of squares	Mean square	F	P	% of contribution
AL, mm	2	0.00873	0.00436	1.89	0.178	1.4
WC Amps	2	0.52544	0.26272	113.48	0.000	87.0
WS, mm/min	2	0.06993	0.03496	15.10	0.000	11.6
Error	20	0.04630	0.00232			
Total	26	0.65040		130.39		100.00

Table 12 Experimental and predicted GRG

Trial no.	Experimental GRG	Predicted GRG	% Error
1	0.4387	0.4689	− 6.43
2	0.4114	0.4071	1.07
3	0.4086	0.3453	18.34
4	0.5893	0.6309	− 6.59
5	0.4794	0.5691	− 15.80
6	0.4511	0.5073	− 11.10
7	0.9333	0.7929	17.71
8	0.7682	0.7311	5.07
9	0.6591	0.6693	− 1.52
10	0.4380	0.4470	− 2.01
11	0.4114	0.3852	6.81
12	0.4044	0.3234	25.08
13	0.5239	0.6090	− 14.00
14	0.4754	0.5472	− 13.10
15	0.4439	0.4854	− 8.53
16	0.8783	0.7710	13.92
17	0.7115	0.7092	0.32
18	0.6144	0.6474	− 5.09
19	0.4294	0.4251	1.02
20	0.4105	0.3633	13.00
21	0.4000	0.3015	32.67
22	0.5000	0.5871	− 14.80
23	0.4627	0.5253	− 11.90
24	0.4390	0.4635	− 5.27
25	0.7983	0.7491	6.57
26	0.7079	0.6873	2.99
27	0.5977	0.6255	− 4.43

(Fig. 7) and 0.9537, 0.961 and 0.9586 (Fig. 8) for the AL of 3 mm, 4 mm and 5 mm, respectively. By employing activated flux, there is a rise in thermal input trailed by TIG welding process. Furthermore, it was perceived that an increase in the WC resulted in a rise in thermal input, which caused a large amount of metal to melt, with the result that increased DOP and corresponding BW were observed in the weld.

It should also be noted that as the AL increases, a decrease in thermal input results in a reduction in DOP and BW. Hence, the influence of thermal input on DOP and BW for respective input parameters such as high WC, low WS and minimum AL is the optimal choice of input parameters to produce high-quality weldments with more DOP and corresponding BW.

3.7 A-TIG welding butt joint configuration

Once the optimal set of input process parameters are optimized to achieve complete penetration of 6-mm-thick plate from the 27 trials, its macrostructure has to be visually examined. With the data presented in Table 9, the respective input parameters have been selected to achieve the full depth penetration for SS321 material of 6 mm thickness by applying EWI flux. Base metal plate of $100 \times 100 \times 6$ mm cross section is put together to fabricate butt joint. Figure 9 shows the butt joint with uniform weld bead surface. Figure 10 shows the macrostructure of the butt joint captured by a stereotype microscope at a magnification of 7×.

3.8 Confirmation test

After calculating the optimum parameters, the next phase is to use the best combination of parameters to determine

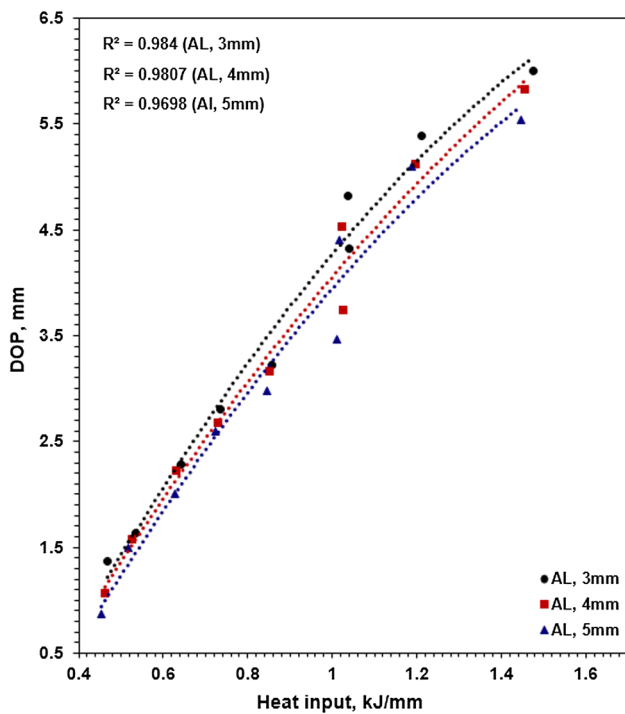**Fig. 6** Experimental and predicted values of GRG
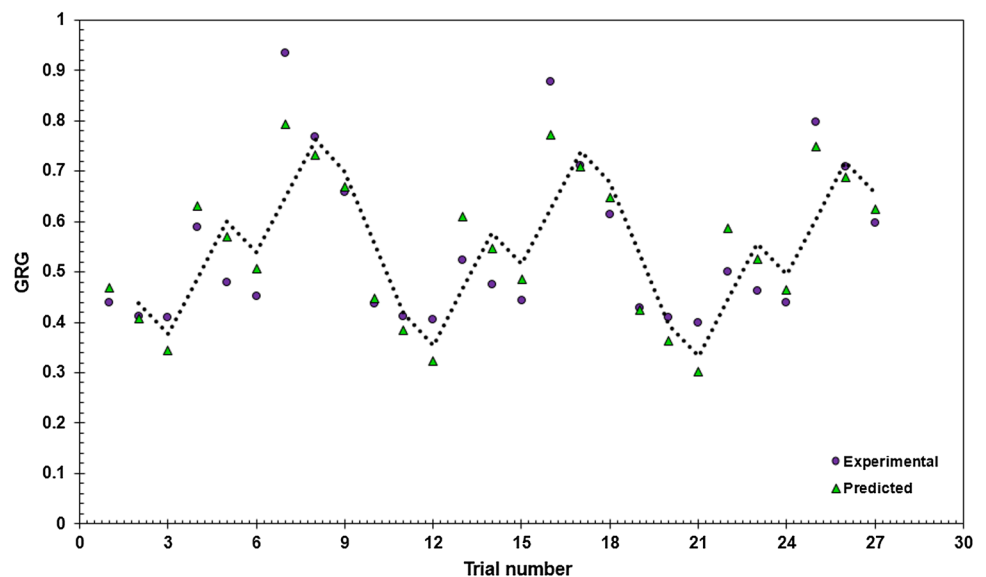
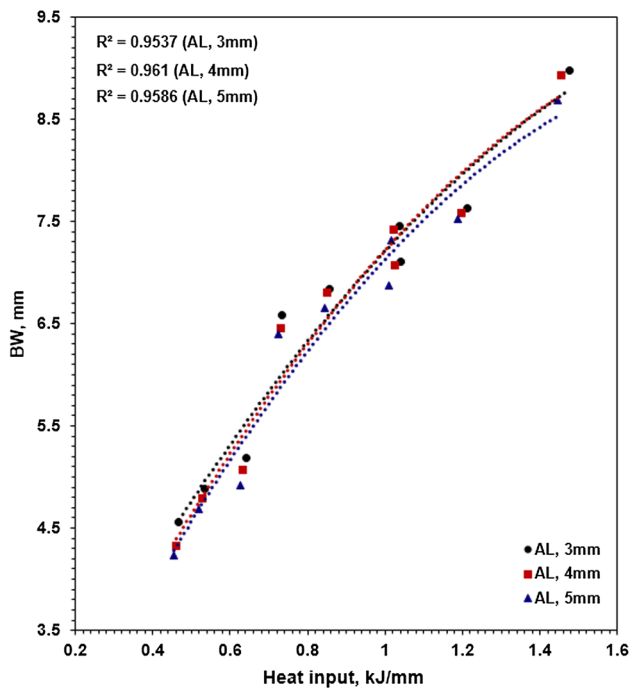Fig. 7 Heat input effect on DOP at different ALs

Fig. 8 Heat input effect on BW at different ALs

and confirm the improvement in the weldment quality. The estimated GRG $\hat{\gamma}$ which uses the optimal level of design parameters can be determined as:
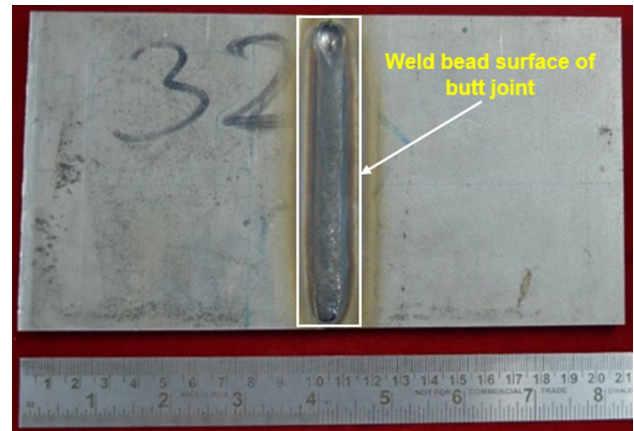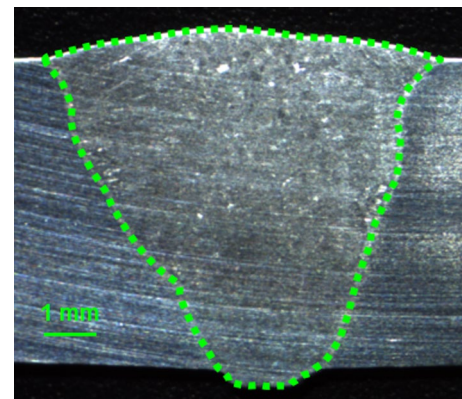

Fig. 9 Butt joint

Fig. 10 Butt joint macrostructure

$$\hat{\gamma} = \gamma_m + \sum_{i=1}^{o} \overline{\gamma}_j - \gamma_m$$
$$= 0.5476 + (0.5711 - 0.5476) + (0.7410 - 0.5476)$$
$$+ (0.6144 - 0.5476) = 0.8313 \tag{11}$$

where γ_m = total mean GRG, $\overline{\gamma}_j$ = mean GRG at the optimal level and o = number of the major design parameters that affect the quality of the weld characteristics. An experiment with the confirmation of welding was carried out during the A-TIG welding using the optimal set of parameters, that is, the AL of 3 mm, the WC of 220 Amps and the WS of 120 mm/min. The values of the weld geometry, obtained with the optimal parameters, are given in Table 13. Table 13 shows a comparison of the predicted DOP and BW with the actual value using the optimum welding conditions. There was a good match between the actual and the predicted results. (The overall GRG improvement was 0.4959 (53%).) The macrostructure of the butt joint, made using the optimal input parameters, is depicted in Fig. 10. The macrostructure of the weldment is uniform without defects such

Table 13 Results of confirmation test

	Initial factor setting	Optimal process parameters	
		Prediction	Experiment
Factor level	$A_1B_1C_1$	$A_1B_3C_1$	$A_1B_3C_1$
DOP, mm	2.2826		6.3400
BW, mm	5.1827		8.6570
GRG	0.4387	0.8313	0.9346

Improvement in GRG = 0.4959

as cracks and porosity. For these sets of parameters, a GRG is calculated, and the value is 0.9346, which is the maximum among all the other 27 experimental parameters. This confirms, for this set of conditions, the correct optimization of the parameters. From the analysis of the geometry of the weld bead, the penetration depth in this case is maximal. It can also be understood that the penetration in this case from the macrostructure (A-TIG welding) is maximum.

4 Mechanical properties and microstructure examination of the butt joint

Generally, austenitic stainless steel weldments have an austenitic matrix with varying amounts of delta ferrite. The amount of delta ferrite in the weld reduces toughness, ductility and corrosion resistance [43]. It is needed to evaluate the mechanical properties and microstructural analysis of butt joint produced by optimized set of input parameters.

4.1 Mechanical properties

The uniaxial tensile test is one of the well-known mechanical tests preferred to qualify welding procedures. Tensile testing provides data on the material strength and ductility under uniaxial tensile stress. This information can be used to compare materials in the field of design, quality control and alloy development in some cases. The samples are prepared for tensile testing as per ASTM E8/8 M-16a standard. The tests were conducted using 50-kN load cell with a Tinius Olsen universal testing machine at a constant loading rate of 1 mm/min. The graphical representation of engineering stress vs. strain plot is shown in Fig. 11. The joint efficiency of the A-TIG welding is 101.12%.

The tensile strength of WM (624 MPa), which is higher than that of BM (621 MPa), and the ductility of WM (45.44%) is reduced compared with that of BM (51.52%). Also, the outcomes of ferrite measurement (make: Fischer Feritscope FMP30) display that the amount of ferrite in the WM (5.9 FN) is higher compared to that in the BM (1.2 FN). Therefore, the increase in tensile strength and reduction in ductility in the WM are attributed to the increase in delta ferrite, especially for steels having a 3 or more percentage of delta ferrite [44]. The equiaxed dendritic structure with increased delta ferrite leads to an increase in the tensile strength [45]. The presence of TiC particles in the WM also
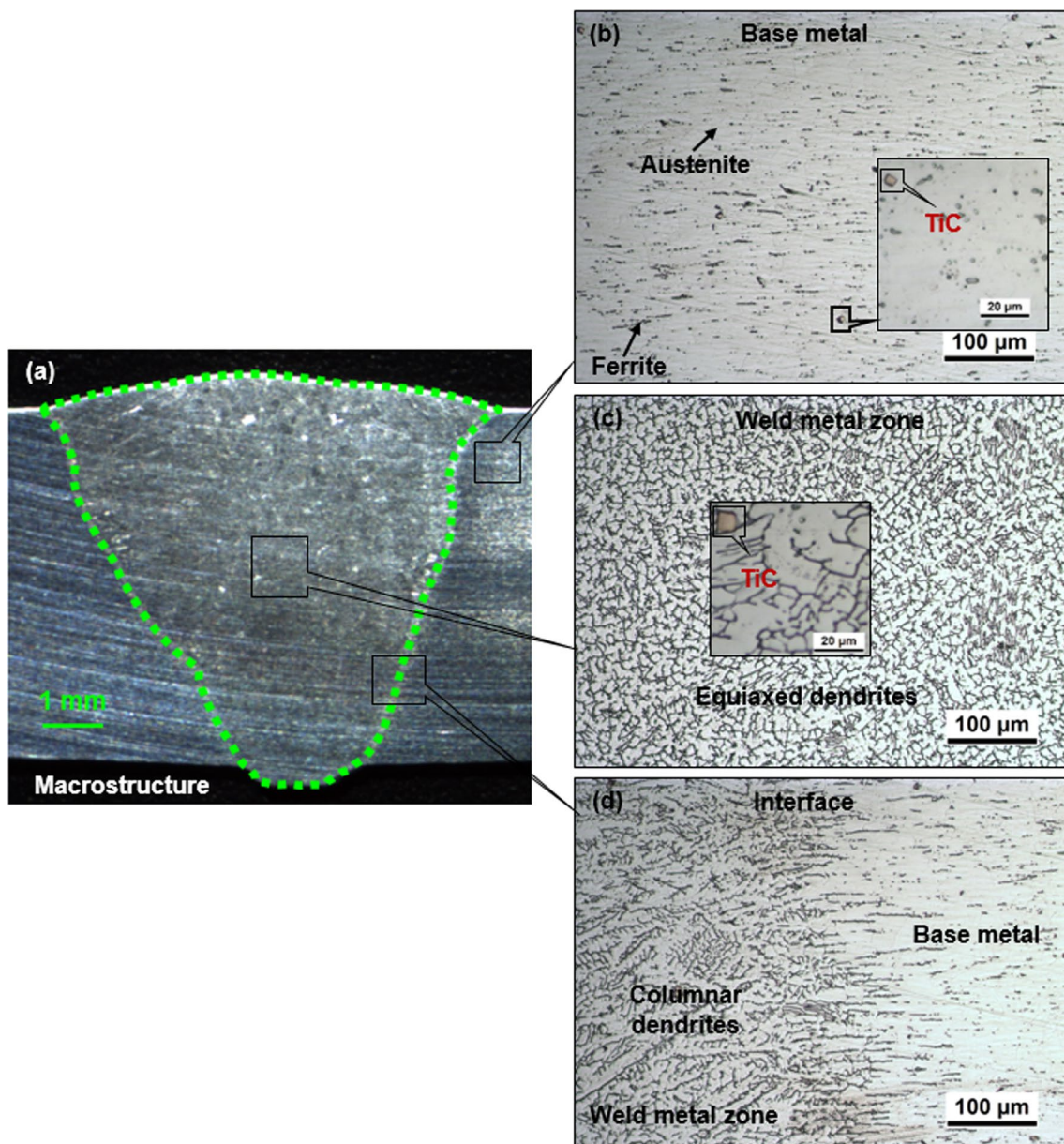
Fig. 11 Graphic of uniaxial tensile test
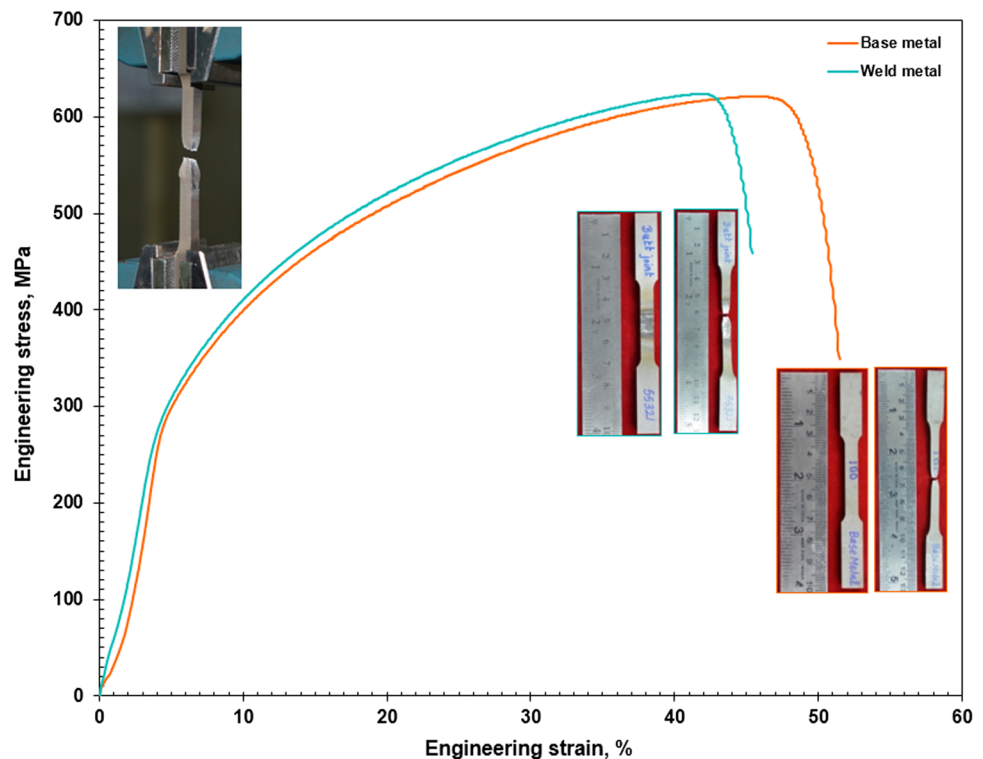
Fig. 12 **a** Macrostructure and optical micrographs of the **b** BM, **c** WM and **d** interface

leads to reduced ductility of weldments. Besides, from the experimental observation, it is indicated that the position of fracture is in the BM region, confirming the welding procedures followed in this study offer superior tensile properties compared to the BM. In order to ensure the ductility of the specimen, the bend test specimen (ASTM E190-14) was subjected to 180° bend. After the test, there were no visible cracks on the surface of the weld, which indicates that the WM has comparable ductility. The Charpy impact test sample is prepared according to ASTM E23-16b. The energy absorbed for the WM (113.46 J) is less than that of the BM (123.17 J), approximately 92.1% of the latter. This

is the reason for the lower impact value of WM compared to that of the BM; WM contains oxide flux-induced inclusions and more ferrite than BM, and the toughness of the ferrite is lower than that of the austenite [46].

4.2 Microstructural examination

Figure 12a shows the macrostructure of the butt joint. The joint consists of BM, WM and interface zone as presented in Fig. 12b–d. The BM microstructure (refer zone b in Fig. 12) comprises austenite and ferrite phase at the grain boundary. BM also shows the presence of titanium carbides
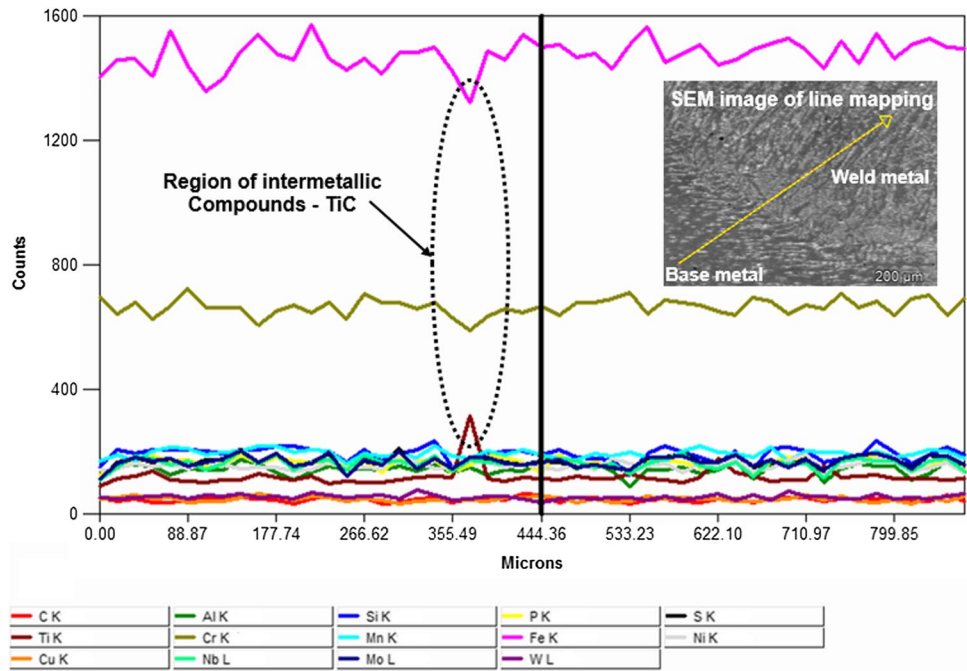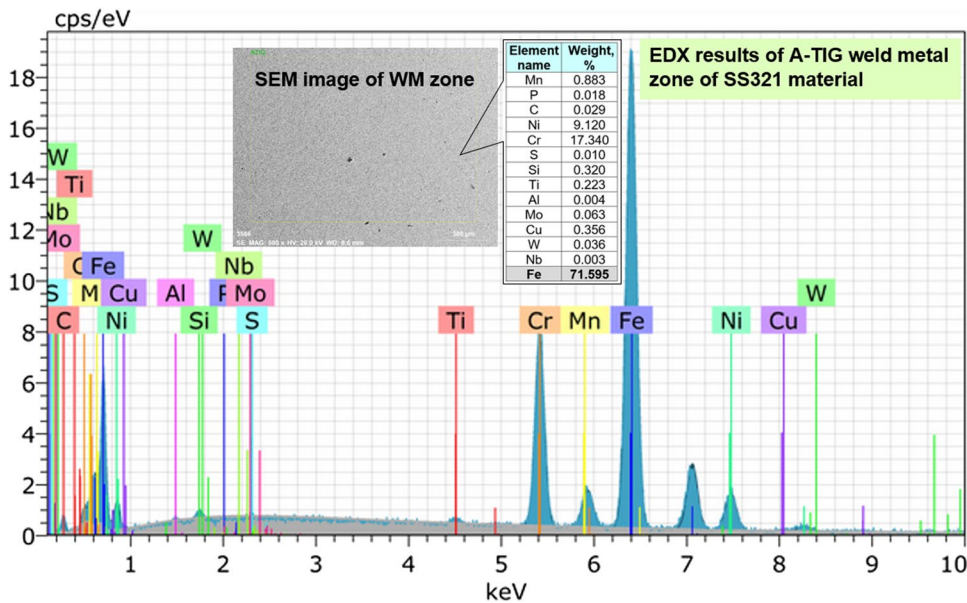
Fig. 13 EDX elemental line scan

Fig. 14 EDX analysis of WM

(TiC)-intermetallic compounds in small level, primarily at grain boundaries [47]. The microstructure of the c–d zone in Fig. 12 reveals that the WM is composed of planar, cellular, columnar and equiaxed dendrites growth. The morphology of the dendrite is primarily decided by G-temperature gradient, R-solid–liquid (S–L) interface rate and degree of constitutional supercooling. G/R decreased from the melting boundary to the internal molten pool, while the degree of constitutional supercooling increased, resulting in the transformation of the solidification mode from planar, cellular, columnar to equiaxed dendrites growth [48]. Further,

the WM region is composed of austenite and a delta ferrite phase. During cooling, the primary delta ferrite solidifies in the WM zone, and then, the transformation delta ferrite → austenite occurs. Since the delta ferrite → austenite transition is a diffusion control process, the higher cooling rate (low heat input) in the A-TIG welding process does not provide sufficient time to complete the phase transition and a small level of delta ferrite is retained in the WM. This phenomenon increases the ferrite wt%. Delta ferrite in the range of 3–8% is required to avoid the formation of hot cracks during solidification of the weld [49, 50]. Not all observed

Fig. 15 WRC-1992 diagram
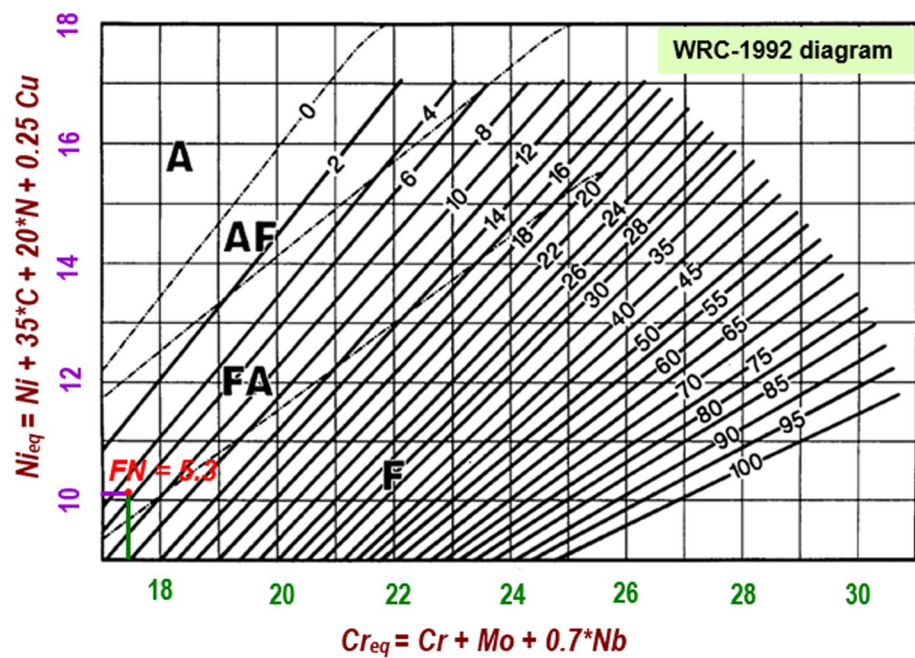
Table 14 FN-measured versus predicted (according to the WRC-1992 diagram)

Material zone	FN—measured	FN—calculated	Measured minus calculated
WM	5.9	5.3	0.6

TiC particles are located at the centre of equiaxed dendrites, which indicates that not all particles act as nucleants [51, 52]. Ferrite dendrites can be clearly observed in a range of around 100 μm from the solidification interface. Austenite is solidified in succession to the retained liquid phase at the ferrite–dendrite boundaries. This result shows that the mode of solidification is FA mode, in which primary phase is ferrite and the secondary phase is austenite during WM solidification [53].

These microstructural features are in line with the previous investigations on austenitic stainless steel weldments by Chandrasekar et al. [54] and Masoud Sabzi et al. [55]. Mehran Nabahat et al. [45] reported that the SS321 WM solidification mode was FA with equiaxed grains at the centre of the fusion zone and columnar dendrites at the interface. Equiaxed dendrites nucleate at the centre of the fusion zone as a result of the heterogeneous nucleation from fragmented dendrites or detached grains. Similarly, the dissolution of TiC in the microstructure confirms that the welding process encompasses the formation of TiC and thereby it retains the Cr wt% [54]. This confirms that heat input plays an important role in the solidification mode and microstructure in weldment. Figure 13 displays the energy-dispersive X-ray

(EDX) elemental line scan from BM to WM region. The distribution of elements in the line illustration shows that Fe and Cr are peaking in the WM than other elements. The results show that when the peaks of Fe and Cr elements decrease and the peak of Ti element increases, it is showing that there is a TiC particle formation in that zone. It is thus obvious that TiC particles present in the WM area avoid weld decay and act as a nucleation site. In addition, this leads to grain growth in the WM [26]. EDX analysis at the WM is shown in Fig. 14. From the results obtained, it is clear that there were no notable changes in the elemental composition in the WM. In addition, there is a small increase in the iron (Fe) content at the WM due to the presence of higher delta ferrite content.

The microstructure of austenitic stainless steel-welded metal depends only on the solidification mode. Typically, the composition in 300 series stainless steel and the equivalent (eq) Cr/Ni range allow all four types of solidification modes to exist, namely austenite—A: $Cr_{eq}/Ni_{eq} < 1.25$), austenite + ferrite—A + F: $1.25 < Cr_{eq}/Ni_{eq} < 1.48$, ferrite + austenite—F + A: $1.48 < Cr_{eq}/Ni_{eq} < 1.95$ and ferrite—F: $1.95 < Cr_{eq}/Ni_{eq}$ (according to the welding research council (WRC)-1992 diagram). This creates difficulty in identifying the WM microstructure, especially when its composition lies close to the eutectic point. According to the WRC-1992 diagram (Fig. 15), the calculated $Cr_{eq} = 17.4$, $Ni_{eq} = 10.2$ and $Cr_{eq}/Ni_{eq} = 1.7$, respectively, for WM using EDX results. Therefore, the solidification mode of WM must be the FA mode: $1.48 < Cr_{eq}/Ni_{eq} < 1.95$. The measured and predicted FN using Feritscope and WRC-1992 in WM is shown in Table 14, and it clearly indicates the higher wt%
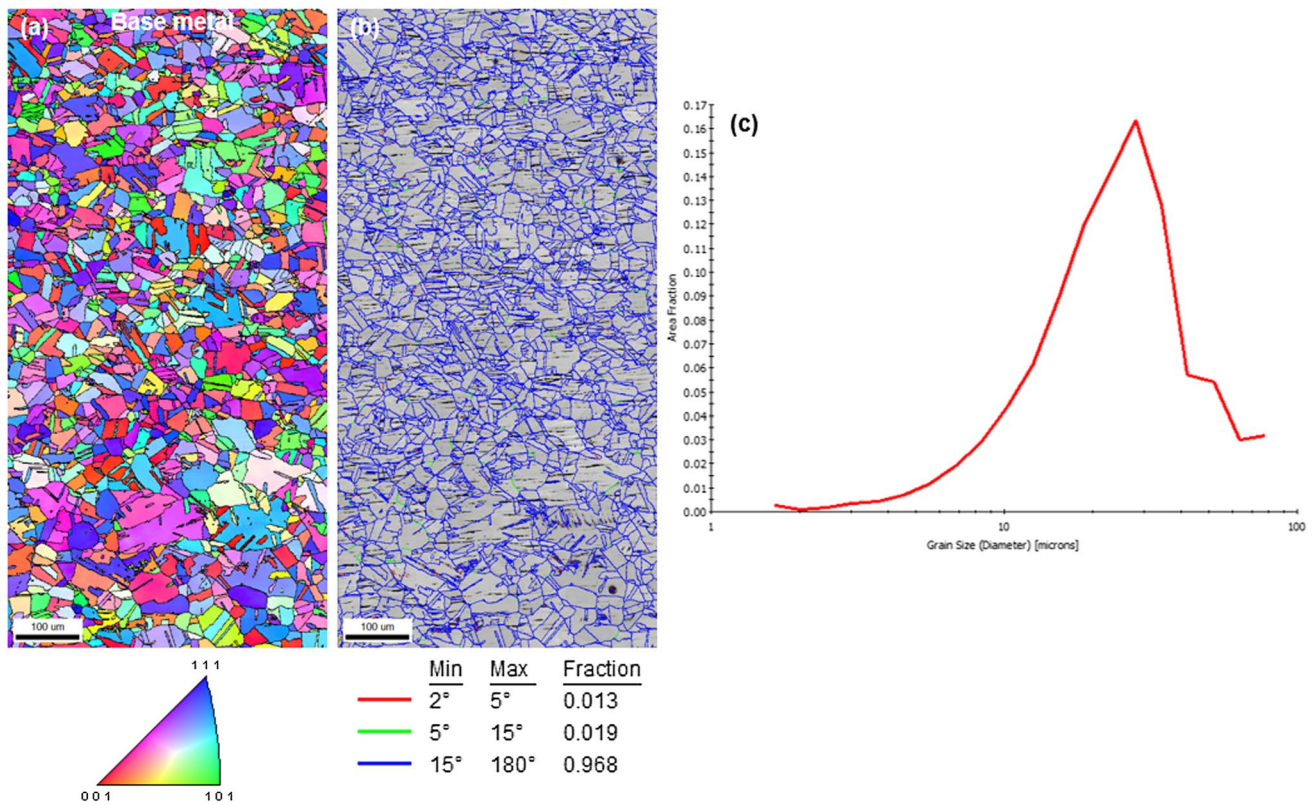
Fig. 16 EBSD images of the BM **a** IPF map, **b** grain boundary map and **c** grain size distribution

of Fe with a deviation of 0.6 FN. The increase in delta ferrite in the weldment will improve the mechanical integrity of the welded joint [56].

The inverse pole figure (IPF) map, grain boundary map and grain size distribution of the BM, interface and WM zones are shown in Figs. 16, 17 and 18. The BM consists of fine grains exhibiting random orientation colour distribution (Fig. 16a), and the average grain size is about 21 μm (Fig. 16c). Table 15 shows the summarized EBSD results of BM, interface and WM zones. The BM constituted 97.0% and 3.0% fraction of high-angle grain boundaries (HAGBs) and low-angle grain boundaries (LAGBs), respectively. It is observed from Figs. 17a and 18a the presence of coarse columnar dendrites and equiaxed dendrites at the middle of the joint, respectively. From Table 15, it can also be seen that interface and WM have a lower fraction of HAGBs compared to BM. Furthermore, Figs. 16c, 17c and 18c show the grain size distribution of BM, interface and WM zones, respectively.

The grain coarsening is attributed to heat input produced during the welding process as initially the grains at the interface grew on the basis of the initial grain. Further, during the welding process the cooling rate is more in WM and temperature gradient at the edge and weld centre is fairly large. Hence, the columnar and equiaxed grains grow along the

direction of the maximum temperature gradient. The average grain size of interface and WM zone is 40 μm and 61 μm, respectively. Figures 16b, 17b and 18b show the grain boundary map obtained from EBSD. The grain boundary misorientation angle distribution has major influence on the mechanical properties specifically for polycrystalline materials. Two types of LAGBs are indicated in red ($2° \leq \theta \leq 5°$) and green colour ($5° \leq \theta \leq 15°$). Boundaries beyond $\theta \geq 15°$ are called HAGBs, which is indicated in blue colour. The increase in tensile strength is mainly based on the LAGBs in the WM when compared with BM. It is observed that LAGBs form within the grain interior as subgrain or dislocation walls and the reason for their formation is the decrease in energy stored to sustain some form of structural integrity at the boundary. LAGBs have a discrete dislocation array, while HAGBs generally keep a disordered structure. As the LAGBs density increases, these dislocation walls are refined, obstructing the movement of slip dislocations, i.e. mobile dislocations across the boundaries, resulting in strengthening of the welded joint when stress is applied. The rise in tensile strength is due to the movement of LAGBs cells as a single unit because of application of stress [57]. The movement of the LAGBs units is dependent on the speed with which the dislocations in the boundary can experience 'climb' [58]. As HAGBs can hinder the expansion of brittle cracks, Σ3
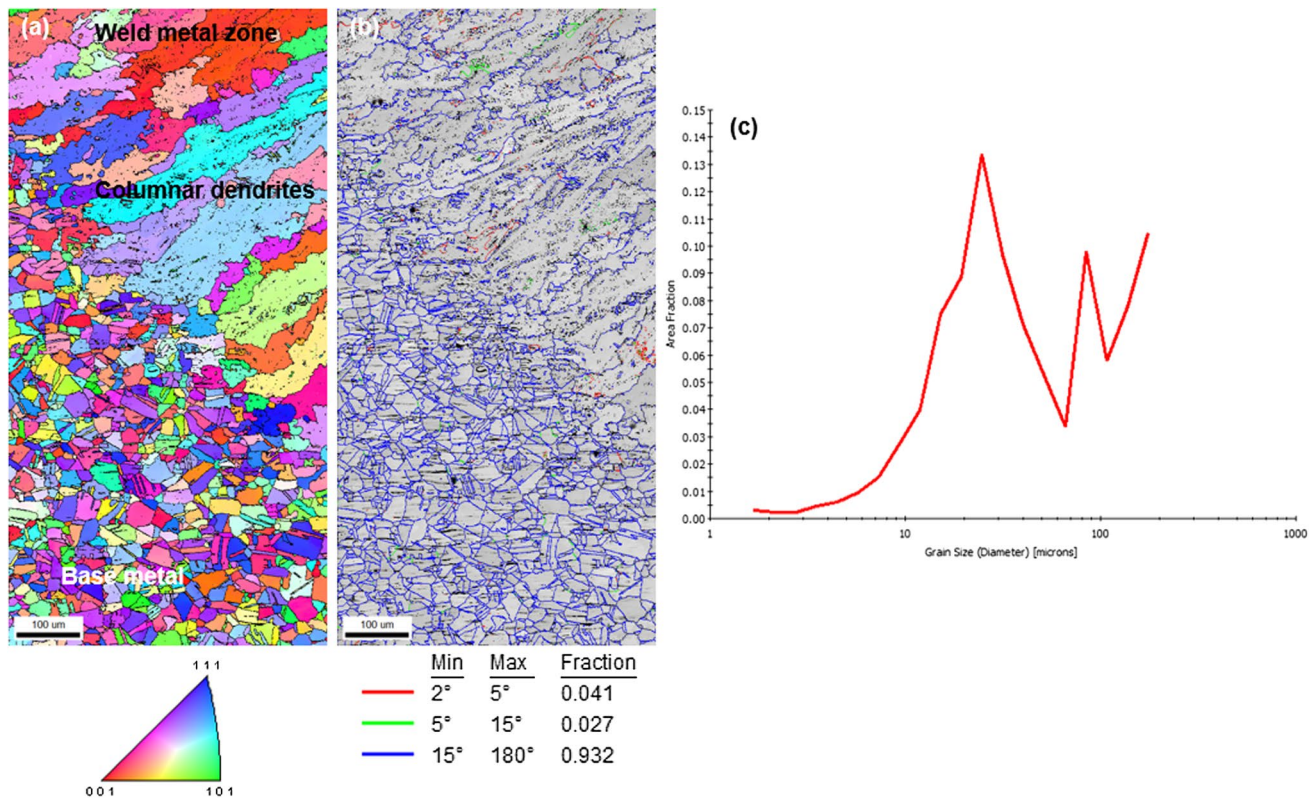
Fig. 17 EBSD images of the interface **a** IPF map, **b** grain boundary map and **c** grain size distribution

($\theta = 60°$) coincidence site lattice boundary (CSL) is a type of distinct grain boundary with fairly low grain boundary energy and lesser impurity segregation. Higher the $\Sigma 3$ CSL boundaries are present, the more impediments there are in the offset of the WM grains which has preferred orientation. Due to the application of the thermal weld cycle, the $\Sigma 3$ CSL boundaries declined significantly and the ability to avert migration of HAGBs decreased. The misorientation angle distribution progressively migrated from HAGBs to LAGBs. In combination with the above examination, it can be stated that for WM compared with BM the tensile strength increases and toughness decreases [59].

4.3 Fractographic examination of samples from uniaxial tensile and impact test

The fractured surfaces of both BM and WM (uniaxial tensile and impact test) samples were investigated using SEM to study the microcharacteristics. SEM photomicrographs show the existence of fine dimples, voids, riverine and honeycomb structure in the BM and WM (Fig. 19). It could be concluded that the nature of the fracture was ductile mode. The fracture surface of the WM shows the existence of microvoids and fine dimples comparing with the BM, and this microvoids aid in the improvement in the load-carrying capacity

of the WM [60–62]. Therefore, it is revealed that the tensile strength of WM (consisting of austenite and delta ferrite phase) is higher than that of BM (predominantly austenite phase with lower amount of delta ferrite). The ductile mode of failure is characterized with sufficient plastic deformation [63]. As the A-TIG tensile sample contains relatively hard oxide inclusions which do not deform at the same rate as the matrix, voids are nucleated in the BM region to accommodate the incompatibility. The ductile mode of failure in austenitic stainless steels consists of the following mechanisms: nucleation growth and coalescence of fine dimples and microvoids [64]. The ductile fracture propagates slowly and after sufficient plastic deformation above the tensile strength. This tensile stress aids in the formation of fine dimples and microvoids at the necking region and interconnects them until fracture by initiating fine crack slowly [65]. Most of the metals, especially with FCC phase such as austenitic stainless, typically have a "cup-cone" fracture at room temperature. Also, the fractured surface of BM and WM impact samples has similar features (dimples, voids, riverine and honeycomb structure), indicating the ductile type of failure (Fig. 20). Further, oxide flux-induced inclusions and higher content of delta ferrite in the austenitic stainless steel weldments reduce the toughness of the WM [46, 66].
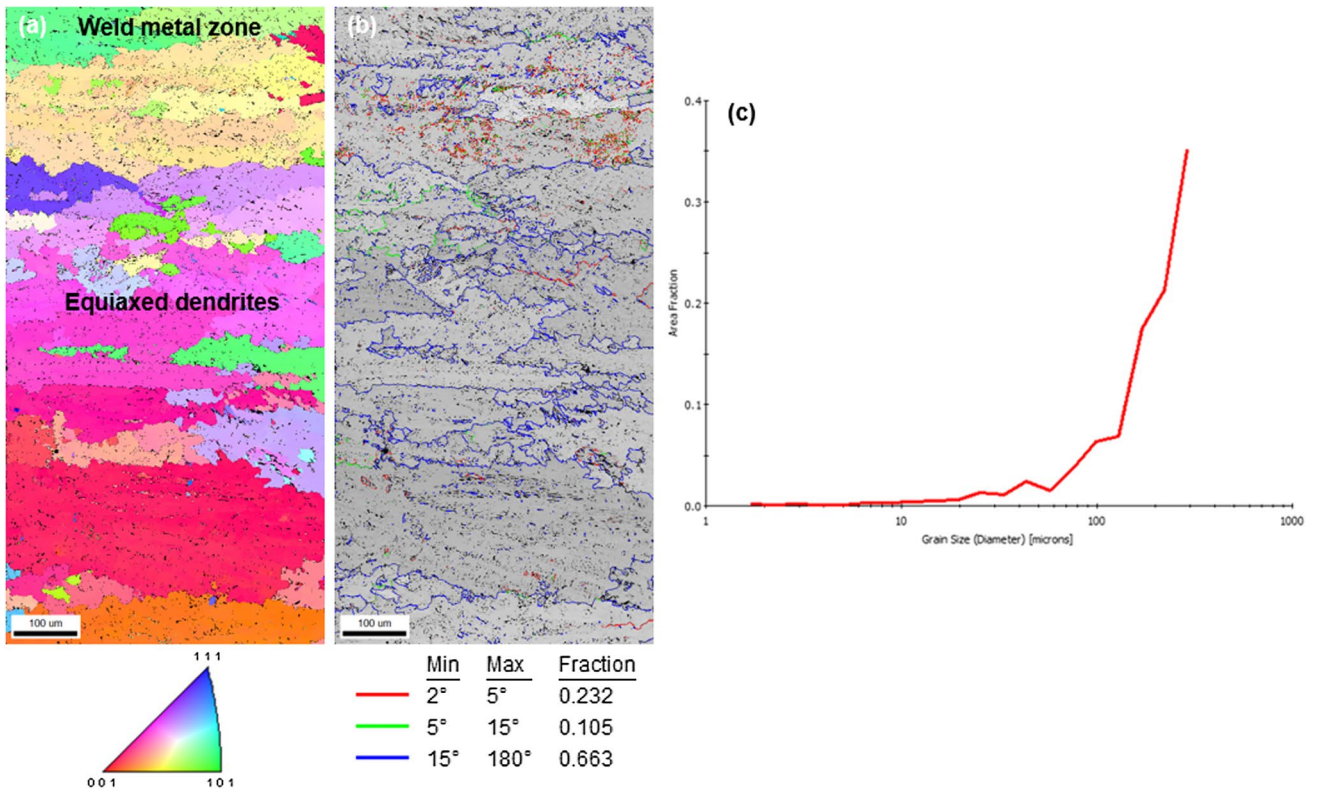
Fig. 18 EBSD images of the WM **a** IPF map, **b** grain boundary map and **c** grain size distribution

Table 15 Grain size, LAGBs and HAGBs of different zones

Region	Average grain size, μm	LAGBs, %		HAGBs, %
		$2° \leq \theta \leq 5°$	$5° \leq \theta \leq 15°$	$15° \leq \theta \leq 180°$
BM	21	1.3	1.9	96.8
Interface	40	4.1	2.7	93.2
WM	61	23.2	10.5	66.3

5 Conclusions

In this current study, the meticulous approach of Taguchi-based GRA optimization technique has been implemented for finding the optimal combination of parameters to attain adequate weld quality, i.e. DOP and BW of the weldment obtained by A-TIG process, so that the essential condition for producing a good welded joint is to provide full DOP.
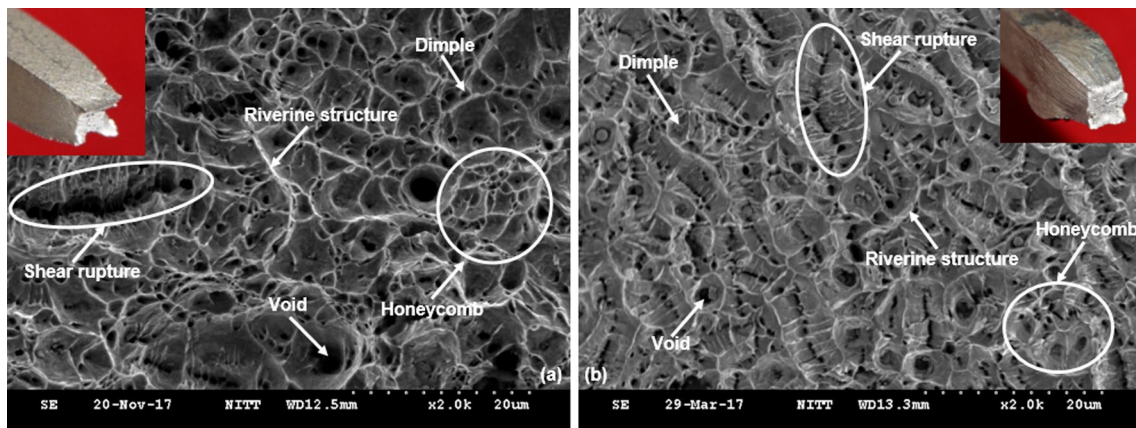

Fig. 19 SEM photomicrograph of the uniaxial tensile fracture surface **a** BM and **b** WM
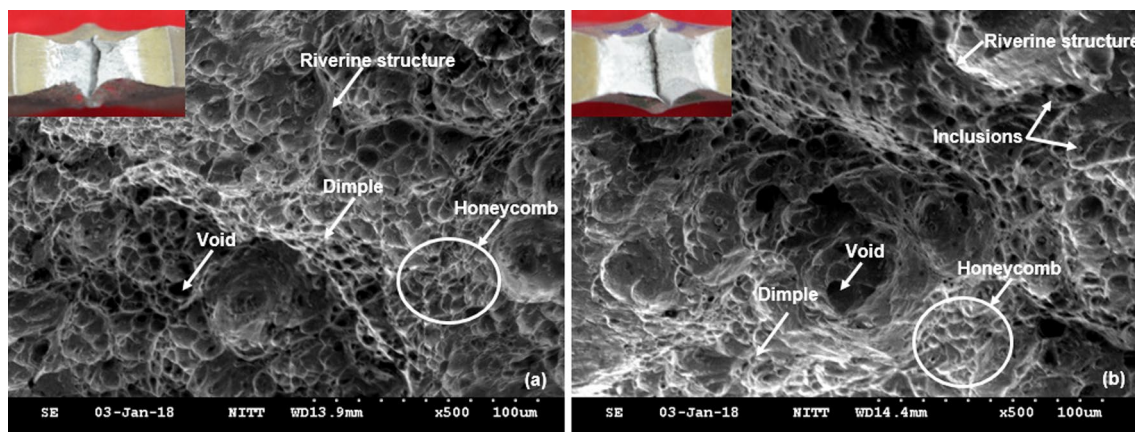
Fig. 20 SEM photomicrograph of the impact test fracture surface **a** BM and **b** WM

Based on the present study, the following inferences are drawn.

- With the help of Taguchi-based GRA optimization technique, to attain the preferred level of quality in weldments, the control of WC is the foremost governing parameter followed by WS and AL.
- From the ANOVA results, it is noted that the percentage of contribution of input parameters, i.e. WC, WS and AL, is 87.0, 11.6 and 1.4, respectively. The optimized input parameter combination is given as follows:

AL, mm	WC, Amps	WS, mm/min
3	220	120

- The effect plots of thermal input during welding process on DOP and BW confirms that high WC, low WS and minimum AL are the ideal choice of choosing the input parameters for the desired weldment with deep penetration and resultant BW.
- An increase in delta ferrite content and oxide flux-induced inclusions reduce the toughness of the joint compared to BM. Also, the butt joint has better tensile strength compared with BM, and this is due to the existence of delta ferrite. After bending test, there are no obvious cracks on the surface of the weldment.
- Microstructure analysis reveals that the WM region of butt joint consists of columnar and equiaxed type dendrite growth. Also, the presence of TiC in the WM will avoid the weld decay and act as nucleate site, leading to grain growth in the WM region.

- EBSD examination confirms that an increase in tensile strength and a decrease in toughness of the butt joint are due to the presence of LAGBs at the centre of the WM during welding process.
- The fracture morphology of the failure surfaces (tensile and impact) indicates that mode of fracture is ductile.

References

1. Nakhodchi S, Shokuhfar A, Iraj SA, Thomas BG (2015) Evolution of temperature distribution and microstructure in multipass welded AISI 321stainless steel plates with different thicknesses. J Press Vessel Technol 137:061405
2. Senior BA (1988) The solidification and in-service transformation behaviour of type 316 and 347 welds fabricated with type 321 Plate. Mater Sci Eng 100:219–227
3. Loureiro A, Rodrigues A (2008) A-TIG welding of a stainless steel. Mater Sci Forum 587–588:370–374
4. Lowke JJ, Tanaka M, Ushio M (2005) Mechanisms giving increased weld depth due to a flux. J Phys D Appl Phys 38:3438–3445
5. Datta S, Bandyopadhyay A, Pal PK (2008) Grey-based Taguchi method for optimization of bead geometry in submerged arc bead-on-plate welding. Int J Adv Manuf Technol 39:1136–1143
6. Esme U, Bayramoglu M, Kazancoglu Y, Ozgun S (2009) Optimization of weld bead geometry in TIG welding process using grey relation analysis and Taguchi method. Mater Technol 43(3):143–149
7. Prasad KS, Chalamalasetti SR, Damera NR (2015) Application of grey relational analysis for optimizing weld bead geometry parameters of pulsed current micro plasma arc welded Inconel 625 sheets. Int J Adv Manuf Technol 78:625–632
8. Juang SC, Tarng YS (2002) Process parameter selection for optimizing the weld pool geometry in the tungsten inert gas welding of stainless steel. J Mater Process Technol 122:33–37
9. Nageshand DS, Datta GL (2010) Genetic algorithm for optimization of welding variables for height to width ratio and application of ANN for prediction of bead geometry for TIG welding process. Appl Soft Comput 10:897–907

10. Kolahan F, Heidari M (2010) A new approach for predicting and optimizing weld bead geometry in GMAW. Int J Mech Syst Sci Eng 2:2

11. Nandagopal K, Kailasanathan C (2016) Analysis of mechanical properties and optimization of gas tungsten arc welding (GTAW) parameters on dissimilar metal titanium (6Al4V) and aluminium 7075 by Taguchi and ANOVA techniques. J Alloys Compd 682:503–516

12. Pan LK, Wang CC, Wei SL, Sher HF (2007) Optimizing multiple quality characteristics via Taguchi method-based Grey analysis. J Mater Process Technol 182:107–116

13. Tamrin KF, Nukman Y, Sheikh NA, Harizam MZ (2014) Determination of optimum parameters using grey relational analysis for multi performance characteristics in CO_2 laser joining of dissimilar materials. Opt Lasers Eng 57:40–47

14. Kim HR, Park YW, Lee KY (2008) Application of grey relational analysis to determine welding parameters for Nd: YAG laser GMA hybrid welding of aluminium alloy. Sci Technol Weld Join 13:312–317

15. Padhi RK, Banerjee AJ, Puri AB (2012) Multi-response optimization of Nd: YAG laser welding using Taguchi method based Grey relational analysis. Elixir Mech Eng 47:8772–8777

16. Hsiao YF, Tarng YS, Huang WJ (2008) Optimization of plasma arc welding parameters by using the Taguchi method with the grey relational analysis. Mater Manuf Processes 23:51–58

17. Gupta SK, Pandey KN, Kumar R (2016) Multi-objective optimization of friction stir welding process parameters for joining of dissimilar AA5083/AA6063 aluminium alloys using hybrid approach. J Mater Des Appl 232:1–11

18. Kasman S (2013) Multi-response optimization using the Taguchi-based grey relational analysis: a case study for dissimilar friction stir butt welding of AA6082-T6/AA5754-H111. Int J Adv Manuf Technol 68:795–804

19. Tarng YS, Juang SC, Chang CH (2002) The use of grey-based Taguchi methods to determine submerged arc welding process parameters in hardfacing. J Mater Process Technol 128:1–6

20. Joseph J, Muthukumaran S (2015) Optimization of activated TIG welding parameters for improving weld joint strength of AISI 4135 PM steel by genetic algorithm and simulated annealing. Int J Adv Manuf Technol 93:23–34

21. Su DWY, Qiu R (2013) The application of orthogonal experiment in development of activating flux for TIG welding. Adv Mater Res 710:182–185

22. Ahmadi E, Ebrahimi AR (2013) The effect of activating fluxes on 316L stainless steel weld joint characteristic in TIG welding using the Taguchi method. J Adv Mater Process 1:55–62

23. Patel AB, Patel SP (2014) The effect of activating fluxes in TIG welding by using ANOVA for SS 321. Int J Eng Res Appl 4:41–48

24. Prasanna J, Karunamoorthy L, Venkat Raman M, Prashanth S, Raj Chordia D (2014) Optimization of process parameters of small hole dry drilling in Ti–6Al–4V using Taguchi and grey relational analysis. Measurement 48:346–354

25. Snow HMM (2002) Investigation of the effect of a surface active flux on the microstructure and properties of gas tungsten arc welds made on a super austenitic stainless steel. Theses Diss 753:1–196

26. Mohan Kumar S, Siva Shanmugam N (2018) Studies on the weldability, mechanical properties and microstructural characterization of activated flux TIG welding of AISI 321 austenitic stainless steel. Mater Res Express 5:1–47

27. MohanKumar S, SivaShanmugam N (2019) Finite element simulation for tensile and impact test of activated TIG welding of AISI 321 austenitic stainless steel. Proc IMechE L J Mater Des Appl 233:2323–2334

28. Taguchi G (1986) Introduction to quality engineering: designing quality into products and processes. Kraus International, White Plains

29. Roy RK (2001) Design of experiments using the Taguchi approach. Wiley, New York

30. Ghosh N, Pal PK, Nandi G (2016) Parametric optimization of MIG welding on 316 L austenitic stainless steel by grey-based Taguchi method. Procedia Technol 25:1038–1048

31. Pal S, Malviya SK, Pal SK, Samantaray AK (2009) Optimization of quality characteristics parameters in a pulsed metal inert gas welding process using grey-based Taguchi method. Int J Adv Manuf Technol 44:1250–1260

32. Deng J (1982) Control problems of grey systems. Syst Control Lett 5:288–294

33. Deng J (1989) Introduction to grey theory. J Grey Syst 1:1–2

34. Tosun N (2006) Determination of optimum parameters for multi-performance characteristics in drilling by using grey relational analysis. Int J Adv Manuf Technol 28:450–455

35. Lin Y-C, Lee H-S (2009) Optimization of machining parameters using magnetic-force-assisted EDM based on grey relational analysis. Int J Adv Manuf Technol 42:1052–1064

36. Sudhagar S, Sakthivel M, Mathew PJ, Ajith Arul Daniel S (2017) A multi criteria decision making approach for process improvement in friction stir welding of aluminium alloy. Measurement 108:1–8

37. Ramesh K, Baranitharan P, Sakthivel R (2019) Investigation of the stability on boring tool attached with double impact dampers using Taguchi based Grey analysis and cutting tool temperature investigation through FLUKE-Thermal imager. Measurement 131:143–155

38. Shanmugarajan B, Shrivastava R, Sathiya P, Buvanashekaran G (2016) Optimisation of laser welding parameters for welding of P92 material using Taguchi based grey relational analysis. Def Technol 12:343–350

39. Sharma A, Yadava V (2011) Optimization of cut quality characteristics during Nd: YAG laser straight cutting of Ni-based super alloy thin sheet using grey relational analysis with entropy measurement. Mater Manuf Processes 26:1522–1529

40. Montgomery DC (1991) Design and analysis of experiments. Wiley, Singapore

41. Kazancoglu Y, Esme U, Bayramoglu M, Guven O, Ozgun S (2011) Multi-objective optimization of the cutting forces in turning operations using the grey-based Taguchi method. Mater Technol 2:105–110

42. Dewan MW, Huggett DJ, Warren Liao T, Wahab MA, Okeil AM (2016) Prediction of tensile strength of friction stir weld joints with adaptive neuro fuzzy inference system (ANFIS) and neural network. Mater Des 92:288–299

43. Kou S (2003) Welding metallurgy, 2nd edn. Wiley, Hoboken, pp 156–160

44. Oru AGGM, Muhamedagi S (2012) Effect of the delta-ferrite content on the tensile properties in Nitronic 60 steel at room temperature and 750 °C. Materials and technology. 46:519–523

45. Nabahat M, Ahmadpour K, Saeid T (2018) Effect of ultrasonic vibrations in TIG welded AISI 321 stainless steel: microstructure and mechanical properties. Mater Res Express 5:1–10

46. Maduraimuthu V, Vasudevan M, Muthupandi V, Bhaduri AK, Jayakumar T (2012) Effect of activated flux on the microstructure, mechanical properties, and residual stresses of modified 9Cr–1Mo steel weld joints. Metall Mater Trans B 43B:123–132

47. Tiamiyu AA, Eskandari M, Nezakat M, Wang X, Szpunar JA, Odeshi AG (2016) A comparative study of the compressive behaviour of AISI 321 austenitic stainless steel under quasi-static and dynamic shock loading. Mater Des 112:309–319

48. Sun J, Ren W, Nie P, Huang J, Zhang K, Li Z (2019) Study on the weldability, microstructure and mechanical properties of thick Inconel 617 plate using narrow gap laser welding method. Mater Des 175:107823

49. Dadfar M, Fathi MH, Karimzadeh F, Dadfar MR, Saatchi A (2007) Effect of TIG welding on corrosion behavior of 316L stainless steel. Mater Lett 61:2343–2346

50. Mirshekari GR, Tavakoli E, Atapour M, Sadeghian B (2014) Microstructure and corrosion behavior of multipass gas tungsten arc welded 304L stainless steel. Mater Des 55:905–911

51. Villafuerte JC, Kerr HW (1990) Grain structures in gas tungsten-arc welds of austenitic stainless steels with ferrite primary phase. Metall Trans A 21A:979–986

52. Green G, Higginson R, Hogg S, Spindler S, Hamm C, Najorka J (2015) Analysis of ferrite formed in 321 grade austenitic stainless steel. Mater Sci Technol 31:418–425

53. Inoue H, Koseki T (2007) Clarification of Solidification behaviors in austenitic stainless steels based on welding process. Nippon Steel Tech Rep 95:62–70

54. Chandrasekar G, Kailasanathan C, Vasundara M (2018) Investigation on un-peened and laser shock peened dissimilar weldments of Inconel 600 and AISI 316L fabricated using activated-TIG welding technique. J Manuf Process 35:466–478

55. Sabzi M, Dezfuli SM (2018) Drastic improvement in mechanical properties and weldability of 316L stainless steel weld joints by using electromagnetic vibration during GTAW process. J Manuf Process 33:74–85

56. Yazdian N, Mohammadpour M, Razavi R, Kovacevic R (2018) Hybrid laser/arc welding of 304L stainless steel tubes, part 2—effect of filler wires on microstructure and corrosion behavior. Int J Press Vessels Pip 163:45–54

57. Singh DK, Sahoo G, Basu R, Sharma V, Mohtadi-Bonb MA (2018) Investigation on the microstructure-mechanical property correlation in dissimilar steel welds of stainless steel SS 304 and medium carbon steel EN 8. J Manuf Process 36:281–292

58. Rollett AD, Gottstein G, Shvindlerman LS, Molodov DA (2004) Grain boundary mobility—a brief review. Z Metallkd 95:226–229

59. Cui S, Shi Y, Sun K, Shengyong Gu (2018) Microstructure evolution and mechanical properties of keyhole deep penetration TIG welds of S32101 duplex stainless steel. Mater Sci Eng A 709:214–222

60. Rajesh Kannan A, Siva Shanmugam N, Arungalai Vendan S (2019) Effect of cold metal transfer process parameters on microstructural evolution and mechanical properties of AISI 316L tailor welded blanks. Int J Adv Manuf Technol 103:4265–4282

61. Mohan Kumar S, Siva Shanmugam N, Sankaranarayanasamy K (2019) Activated TIG welding of AISI 321 austenitic stainless steel for predicting parametric influences on weld strength of tensile test-experimental and finite element method approach. Adv Comput Methods Manuf Singapore 25:179–192

62. Rajesh Kannan A, Siva Shanmugam N (2020) Some studies on mechanical properties of AISI 316L austenitic stainless steel weldments by cold metal transfer process. Adv Addit Manuf Join Singapore. 32:359–371

63. Xin J, Fang C, Huang C, Yang W, Dai W, Zhang H, Wei J, Li L, Jiefeng Wu, Song Y (2019) Analysis of the fracture mechanism at cryogenic temperatures of thick 316LN laser welded joints. Fusion Eng Des 148:1–10

64. Sabzi M, Obeydavi A, Mousavi Anijdan SH (2019) The effect of joint shape geometry on the microstructural evolution, fracture toughness, and corrosion behavior of the welded joints of a Hadfield Steel. Mech Adv Mater Struct 26:1053–1063

65. Sabzi M, Dezfuli SM (2018) Post weld heat treatment of hypereutectoid hadfield steel: characterization and control of microstructure, phase equilibrium, mechanical properties and fracture mode of welding joint. J Manuf Process 33:313–328

66. Khalifeh AR, Dehghan A, Hajjari E (2013) Dissimilar joining of AISI 304L/St37 steels by TIG welding process. Acta Metall Sin (Engl Lett) 26(6):721–727